Design of hearing aid shells by three dimensional laser scanning and mesh reconstruction

Gabriella Tognola
Consiglio Nazionale delle Ricerche
Istituto di Ingegneria Biomedica
Piazza Leonardo da Vinci, 32
I-20133 Milan
Italy
E-mail: Gabriella.Tognola@polimi.it

Marta Parazzini
Consiglio Nazionale delle Ricerche
Istituto di Ingegneria Biomedica
Piazza Leonardo da Vinci, 32
I-20133 Milan
Italy
    and
Politecnico di Milano
Dipartimento di Bioingegneria
Piazza Leonardo da Vinci, 32
I-20133 Milano
Italy

Cesare Svelto
Politecnico di Milano
Dipartimento di Elettronica e Informazione
CNR-IEEIT and INFM
Via Ponzio 34/5
I-20133 Milan
Italy

Manuela Galli
Politecnico di Milano
Dipartimento di Bioingegneria
Piazza Leonardo da Vinci, 32
I-20133 Milano
Italy

Paolo Ravazzani
Ferdinando Grandori
Consiglio Nazionale delle Ricerche
Istituto di Ingegneria Biomedica
Piazza Leonardo da Vinci, 32
I-20133 Milan
Italy

Abstract. Hearing aid shells (or earmolds) must couple the hearing aid with the user's ear. Earmolds have to fit the subject's outer ear canal properly to ensure a good performance of the aid. Because of the great variability in the anatomical pattern of the ear, earmolds are custom made. At present, an impression of the subject's ear canal is taken and used to fabricate the silicon-made mold. The postimpression activities that typically are performed during the fabrication process modify the physical dimensions of the resulting earmold and thus affect the fit of the product. A novel system for 3-D laser scanning and mesh reconstruction of the surface of ear canal impressions is presented. The reconstructed impression can be digitally stored and passed directly to dedicated CAD 3-D printing machines to model the silicon earmold and thus achieve the best possible fit. The proposed system is based on a couple of cameras and a commercial laser for the surface digitization and on a straightforward algorithm, based on the deformation of a geometric model, for the reconstruction of the acquired surface. Measurements on objects of well-known geometric features and dimensions are performed to assess the accuracy and repeatability levels of this 3-D acquisition system. Robustness to noise of the proposed reconstruction algorithm is determined by simulations with a synthetic test surface. Finally, the first measurements (acquisition+reconstruction) of closed surfaces from ear canal impressions are reported. © 2004 Society of Photo-Optical Instrumentation Engineers.
[DOI: 10.1117/1.1756595]

1 Introduction

The hearing aid shell (or earmold) couples the sound amplified by the hearing aid to the eardrum. Proper fitting to the subject's ear canal is required to achieve satisfactory wearing comfort for an extended period of time, retention of the aid in the ear, reduction in acoustic feedback caused by the leakage of amplified sound inside the earmold, and to avoid unwanted electroacoustic changes in the sound produced by the aid. All these aspects may cause significant discomfort for the user in hearing sounds amplified by the aid.

Because of the great variability in the shape of the ear canal, the majority (over 80%) of all earmolds are custom made. To date, the hearing aid shell is industrially fabricated as a replica of the impression of the subject's ear canal obtained by pushing a malleable material into the ear until it sets. The final silicon-cast hearing aid shell is obtained at the end of a multistep process that includes coating with wax to erase surface imperfections, the production of a reverse image of the original impression, called investment cast (which reproduces the contour of the patient's ear canal), and pouring the material that hardens into the final shell.

All these postimpression processes modify the physical dimensions and the shape of the final product and can thus affect both wearer comfort and susceptibility to acoustic feedback. It should be noted that changes in the shape of the earmold can produce significant discomfort to the user. Also, because the shell fabrication process is fully manual, the quality of the fit of the final product strictly depends on the skills

Address all correspondence to Dr. Gabriella Tognola, Politecnico di Milano, Istituto di Ingegneria Biomedica CNR, Piazza Leonardo da Vinci, 32, I-20133 Milano, Italy. Tel: 39-022399-3388; Fax: 39-022399-3367; E-mail: Gabriella.Tognola@polimi.it

of the technician; in other words, the fabrication process cannot be repeated consistently. Additional difficulties in achieving the optimal fit of earmolds are due to the shrinkage of the impression material over time. The shrinkage is present as early as two days after the impression has been taken. For this reason, the time between the production of the impression and the fabrication of the earmold has to be very short.

The approach described here may contribute to overcoming the drawbacks mentioned. Here, the surface of the original ear canal impression is 3-D laser scanned and reconstructed by means of iterative deformations of a geometric model of simple shape. Finally, the triangular mesh thus obtained is smoothed by a nonshrinking low-pass spatial filter, and a fully digital copy of the impression is obtained. This approach has several advantages over the traditional process of manufacturing earmolds. It is no longer necessary to use postimpression processes because the digitally reconstructed impression can be fed directly to ad hoc CAD/CAM 3-D printing machines, thus achieving a better accuracy in obtaining an exact replica of the ear canal. Also, this kind of digital storage of the impression allows a simple and reliable copy or transmission of the model.

In this study, a prototype 3-D scanning system is presented. The physical acquisition system and the surface reconstruction algorithm are described. Measurements on objects of well-known geometric features and dimensions are performed to assess the accuracy and repeatability levels of the 3-D acquisition system. The robustness to noise of the proposed reconstruction algorithm is determined by simulation with a synthetic test surface of a shape and dimension similar to a typical ear canal impression. Finally, the first measurements (acquisition+reconstruction) of various ear canal impressions are presented.

2 The 3-D Scanning System

Current scanning technologies include contact scanners based on mechanical sensors, and noncontact digitizers based on optical technology. Optical technology is generally preferred because it gives a greater flexibility in the digitization of surfaces and provides higher resolution and accuracy than mechanical technology. Optical technology is based mainly on stereovision or laser triangulation. Scanners based on stereovision use 2-D images taken from cameras at different viewing angles to reconstruct the surface of the object. Laser triangulation systems usually provide more accurate results with less computational cost. In these systems, a laser beam is projected on the object and the light backscattered from the object is collected by a sensor (a linear array if a laser dot is used or a CCD camera if laser stripes are projected). A dedicated circuitry measures the 3-D coordinates of the laser spot (or all the points along the laser stripe) on the object.

The scanning device proposed here (see Fig. 1) is based on optical technology composed of a high-quality, but still commercial and low-price helium:neon (He:Ne) laser (Melles Griot model 05LHP121, class IIIa, with 2 mW at 633 nm on a 600-μm spot diameter), two CCD cameras (MacReflex, model 170-157 version NP), and a real-time video processor (model 170-002 version 5.0), both developed by Qualisys (Sweden). Each camera has 604 (H)$\times$294 (V) picture elements and a frame rate of 60 Hz. For a more detailed description of the scanning equipment, see Ref. 1.
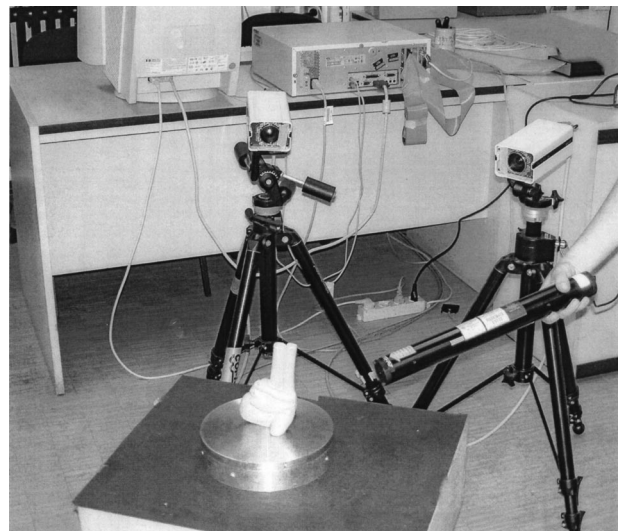

Fig. 1 The optoelectronic 3-D laser scanning system used in this study. Two CCD cameras are put in front of the object to be scanned (here a model of a human heart). The signal coming from the cameras is fed to the video processors (not seen in this picture), which in turn are connected to a personal computer. The object is scanned by manually sweeping the laser beam over its surface.

The digital cameras and the video processor used here are commercial and common equipment used in biomedical laboratories and were developed for wireless 3-D capture of motion. This equipment can measure the 3-D coordinates of a high-intensity light spot. In motion capture, the light spot is produced indirectly by the reflective light from passive retroreflective markers that are stroboscopically illuminated by an array of infrared LEDs arranged in ring form around the lens of the camera unit. Markers are usually made of a common retroreflective material, such as 3M Scotch tape 8850, and are attached by double-sided tape to the body of the moving subject.

In this study, instead of measuring the 3-D coordinates of a retroreflective passive marker, the Qualisys system was used to measure the 3-D coordinates of an ''active'' light spot produced by shining a laser beam over the surface of the object to be scanned. The surface can thus be entirely digitized by manually sweeping the laser over the object. The following subsections give some details (as obtained from the MacReflex Reference Manual and from a scientific publication by Qualisys[2]) on the procedures performed by the Qualisys system to measure the 3-D coordinates of a light spot.

2.1 *Measurement of the 3-D Position of the Light Spot*

The measurement of 3-D coordinates of the light spot is performed in two steps: (1) measurement of the 2-D position of the light spot on the focal plane of each camera and (2) computation of a single 3-D coordinate from the two couples of 2-D positions, (x_1, y_1) and (x_2, y_2), of the laser spot digitized by the two cameras.

The Qualisys video processor performs some dedicated processing on the picture taken from each camera to find the 2-D position of the light spot on the focal plane of the camera. The video processor is able to find the light spot in a picture that is dark elsewhere. In particular, this is achieved by the

use of an electronic shutter and a variable gain. The variable gain allows automatic adjustment of the sensitivity of the camera to match the object with the highest intensity in a way that leaves all other objects dark. This procedure allows suppresses undesired reflections and irrelevant light sources. The video processor scans the picture processed by the cameras. The picture is divided into rows and columns and the transition between dark (i.e., the background) and light is detected together with the light intensity of each pixel. This information on the border position and pixel intensity is used to determine the 2-D position of the geometric centroid of the marker. Also, to avoid possible incorrect spot detection, only light spots within a user-defined size are accepted. This allows the processor to reject both too large light spots (due to sources different from the laser beam) and too small spots (probably due to noise sources).

To compute the 3-D position of the light spot, the cameras must be linearized and calibrated. The purpose of the calibration procedure is to determine the location and orientation of each camera in use with respect to the working volume, whereas linearization is done to correct the nonlinearities of camera components, such as optical nonlinearities that are due to lens distortion. The calibration procedure performed by the Qualisys software records the positions of four reflective markers put on a specially designed L-shaped rigid matrix and a pair of markers attached at the extremities of a wand randomly moved inside the working volume. During the calibration, the L-shaped matrix is maintained static and is used to set the position of the x-y-z Cartesian axes in the working volume. The distance between the two wand markers determines the scaling of the reference coordinate system. Before starting the calibration, the user must provide the system with the real position of the four static markers and the wand length. The calibration utility operates on the information provided by the distance of the moving marker pair and the locations of the four static markers to determine the location and orientation of each camera. Because the calibration utility makes no assumptions about a camera's orientation, there are no restrictions on the actual implementation. By adjusting the lens, focus, and position of the cameras relative to the object, it is possible to use the same device to scan objects of different sizes, from a minimum calibration volume of about $20 \times 20 \times 20$ cm^3 to the total body. The calibration procedure is completed after approximately 30 s.

2.2 *Registration of Multiple Scans of an Object*

To obtain a complete digitization of the object's surface, often multiple scans from different viewpoints are required. This is because the scanning device can acquire only part of the object at a time and/or the object itself may shadow the laser beam reflected from the scanned surface. During the registration process, the multiple scans of the same object are transformed from the different local coordinate systems to a single coordinate system. The goal of this registration process is to find the best rigid transformation T that transforms the point **p** from view P in the corresponding point **q** from view Q (**p** and **q** represent the same surface point).

In this study, the object is put on a turntable in front of the two stationary cameras. Then, the turntable is progressively rotated by a known rotation angle α to obtain multiple scans of the object at different viewing angles. In this way, the

transformation T corresponds to a simple rotation matrix defined by the rotation angle α about the rotation axis of the turntable.

3 The Reconstruction Algorithm

At the end of the scanning and registration procedures, a set of 3-D coordinates of the different points, $d_i = \{x_i, y_i, z_i\} \in R^3$ on the surface S_o of the object is obtained. The dataset $D = \{d_1, \ldots, d_n\}$ consists of completely unstructured data. In this study, the original surface S_o of the object is reconstructed by means of a triangular mesh model M. The triangular mesh M approximating the surface S_o is obtained through an adaptive deformation of a geometric deformable model.

During the past few decades, geometric deformable models have been extensively used in the reconstruction of 3-D free-form surfaces and 2-D contours (for a comprehensive review on geometric deformable models, see Ref. 3). In all these approaches, the model is iteratively deformed until it minimizes an energy function, which contains particular information corresponding to the surface to be fitted. Computational difficulties, nonstable solutions, and nonconvergence are the problems that may be encountered in the minimization of the energy function. Within the framework of geometric deformable models, Miller et al.,[4] Williams and Shah,[5] and Bulpitt and Efford[6] proposed a simpler algorithm to fit the model to 3-D surfaces. In their approach, each vertex of the model moves toward a new position that minimizes its energy locally and independently from the neighboring vertices, thus achieving a more favorable computational complexity.

Our approach is similar to those described in Refs. 4–6 in the sense that it is based on the deformation of a geometric model but instead of minimizing an energy function, it minimizes an error function. At each iteration, the geometric model is deformed and resampled in a way that locally minimizes an error function, which gives a quantitative estimate of the accuracy of the reconstruction. The error function is used here to obtain a nonuniform triangular mesh M characterized by a greater density of triangles right in those regions of the surface with a higher spatial frequency content.

The algorithm here described was developed for the reconstruction of closed surfaces of genus zero, as is the case of ear canal impressions. By simply changing the shape of the geometric model, as shown in Ref. 1, the proposed method can be generalized for use with open surfaces. The reconstruction is performed in three phases.

3.1 *First Phase—Coarse Approximation of Surface S_o*

During the first phase, a regular geometric model—an icosahedron—is put inside the volume defined by the range data D. The icosahedron is then expanded iteratively until all its vertices reach the boundary of the surface S_o in a way that any further expansion would bring its vertices outside the range data. At each iteration, the expansion is obtained by moving each vertex of a fixed amount—*step*—along the vertex normal, which is the direction given by the vector sum of the normals of the triangles to which the vertex belongs. The effect obtained on the entire geometric model by this deformation is similar to that of an inflating balloon. The number of iterative expansions that each vertex is allowed to perform

depends on how many points of the range data D fall into its neighborhood at each iteration. The vertex neighborhood is defined here as a sphere S_d of diameter d centered at the vertex, where the value of d is set approximately equal to the average spatial density of the range data D. If at the iteration $i+1$ the number of points of D falling into S_d is equal to or greater than the number of points found at iteration i, the vertex model is truly approaching the surface boundary and its new position is retained as valid. If this condition is not satisfied, the new position is not accepted and the vertex remains at the old position assumed at iteration i. At each iteration, the vertex can move along its normal of a $step < d$.

Once the icosahedron has reached its maximum expansion, it is uniformly resampled; each triangular face is divided into four faces by connecting the midpoints of its edges. This is because the icosahedron has an insufficient number of vertices to properly describe the range data, which usually consist of a very high number of points. Usually, two or three global resamplings of the original icosahedron are enough to achieve an initial coarse approximation of the surface S_o, while limiting the computational time headed to deform the resampled model. At each global resampling step, the added vertices are again moved closer to the range data along their vertex normals using the same sphere S_d of diameter d as described before. This procedure gives at the end of the first phase a mesh M_1 that is a coarse approximation of the target surface S_o.

3.2 Second Phase—Mesh Refinement

During the second phase, the mesh M_1 is locally resampled to obtain a mesh M_2 that is richer in details where higher spatial frequencies are present. This nonuniform resampling is obtained by introducing new vertices in those triangles of the mesh M_1 having a relatively higher local approximation error. This error is the distance between the target surface S_o and the surface represented by the mesh M_1. Local resampling takes place at a triangle if its distance from the surface exceeds a predefined threshold value.

Given a point $\mathbf{p}$ and a surface S, the distance $e(\mathbf{p},S)$ is defined as[7]

$$e(\mathbf{p},S) = \min[d(\mathbf{p},\mathbf{p}')], \qquad (1)$$

where $\mathbf{p}' \in S$ and $d(\bullet)$ is the 3-D Euclidean distance between the two points $\mathbf{p}$ and $\mathbf{p}'$. The error E between two surfaces S_1 and S_2 can be defined as:[7]

$$E(S_1,S_2) = \max[e(\mathbf{p},S_2)], \qquad (2)$$

where $\mathbf{p} \in S_1$.

In our case, for each triangle $t_i (i=1,...,m)$ of the triangular mesh M_1 we compute the errors $E_{t_i}^{before}(t_i,S_o)$ and $E_{t_i}^{after}(t_i,S_o)$ between the triangle t_i and the surface S_o (here modeled by the range data) before and after the local resampling of t_i. To compute the error $E_{t_i}^{after}(t_i,S_o)$ after the local resampling of t_i, the added vertices are moved closer to the range data using the same sphere S_d of diameter d and the procedure described in the first phase. The resampling is considered valid if the variation

$$\Delta E_{t_i} = (E_{t_i}^{before} - E_{t_i}^{after})/E_{t_i}^{before}$$

of the local error is greater than a threshold value ΔE_{th}; i.e., when the resampling produces a local significant improvement of the accuracy of the reconstruction. At each local resampling step, the resulting mesh is retriangulated to maintain a correct connection. The refinement process of M_1 is stopped when there are no more triangles to be resampled. The result of the refinement phase is a nonuniform triangular mesh M_2.

3.3 Third Phase—Mesh Smoothing

To further improve the quality of the reconstruction, the mesh M_2 is filtered with the iterative low-pass filter proposed by Taubin.[8] In contrast to the classical Gaussian filter, Taubin's filter does not produce shrinkage of the mesh.

Briefly, if $x=(x_1,...,x_n)^t$ is a discrete surface signal defined on the vertices of a polyhedral surface (such as a triangular mesh), the discrete Laplacian is defined as

$$\Delta x_i = \sum_{j \in i^*} w_{ij}(x_j - x_i), \qquad (3)$$

where i^* is a set of indices of vertices belonging to the neighborhood of the vertex v_i and the weights w_{ij} are equal to the inverse of the number of neighbors $1/|i^*|$ of vertex v_i for each element j of i^*. In the case of a triangular mesh, the neighborhood of the vertex v_i is the set of all the vertices v_j sharing one edge with v_i.

In the classical spatial low-pass Gaussian filter, the new value x_i' of the discrete surface after filtering is computed as

$$x_i' = x_i + \lambda \Delta x_i, \qquad (4)$$

where $0 < \lambda < 1$ is a scale factor. In this case the transfer function of the filter is $f(k) = 1 - \lambda k$. In the filter proposed by Taubin,[8] after performing the Gaussian filter of Eq. (4) with a positive scale factor λ—the shrinking step—for all vertices of the triangular mesh, another similar step—the unshrinking step—is performed using a negative scale factor μ (with $\mu < -\lambda$):

$$x_i'' = x_i' + \mu \Delta x_i. \qquad (5)$$

It can be demonstrated[8] that this smoothing procedure corresponds to the transfer function $f(k) = (1 - \lambda k)(1 - \mu k)$. The passband frequency k_{PB}, such that $f(k_{PB}) = 1$, is

$$k_{PB} = \frac{1}{\lambda} + \frac{1}{\mu} > 0. \qquad (6)$$

The filter can be iterated N times. In that case, the passband region still extends from $k=0$ to $k=k_{PB}$ where $f(k)^N \approx 1$. For k greater than k_{PB}, the transfer function decreases to zero. The rate of decrease is controlled by the number of iterations N. To implement the filter, first it is necessary to chose a value for k_{PB}, λ, and N. The value for μ can be derived from Eq. (6). To minimize the number of iterations N, λ must be chosen as large as possible, while keeping $|f(k)| < 1$ for $k > k_{PB}$. It can be demonstrated that this constraint is achieved when:[9]
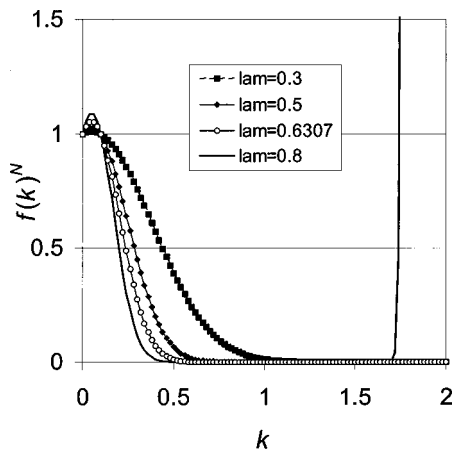
Fig. 2 Graph of the transfer function $f(k)^N = [(1 - \mu k)(1 - \lambda k)]^N$ for different values of the parameter $\lambda = \{0.3, 0.5, 0.6307, 0.8\}$. In all cases, the pass-band frequency k_{PB} was set equal to 0.1 and the number of iterations was $N = 50$. The value $\lambda_{\lim}$ was equal to 0.6996 [as calculated from Eq. (7)]. Note that the greater the value of λ, the steeper the transition band of the filter. For $\lambda > \lambda_{\lim}$, such as for example with $\lambda = 0.8$, the filter becomes unstable. In particular, in the proposed mesh reconstruction algorithm (see Sec. 3.3), we used $\lambda = 0.6307$.

$$\lambda < \lambda_{\lim} = \frac{-k_{PB} + [(2 - k_{PB})^2 + 4]^{1/2}}{2(2 - k_{PB})}. \qquad (7)$$

As an example, Fig. 2 shows how different choices of the parameter λ influence the transfer function $f(k)^N$ of the resulting filter.

While filtering, the vertices are moved without changing the connectivity, the number of vertices and triangles of the mesh. As stated before, the number of iterations and the values of parameters of the filter affect the bandwidth of the filter. To obtain a stable filter, without elongations and ripples in the bandwidth of the transfer function, we used the parameter values originally suggested by Taubin,[8] i.e., $\lambda = 0.6307$ and $k_{PB} = 0.1$. At the end of the filtering process, a new smoothed mesh M_3 is obtained.

4 Results

4.1 Estimation of the System Acquisition Noise and Spatial Resolution During Laser Scanning

All the measurements described in this paper were done using a calibration volume of $30 \times 30 \times 30$ cm^3 and standard Cosmicar 8.5-mm lenses for the cameras, with a horizontal field of view of 39 deg.

In a first set of experiments, a static laser spot was shined on a reference plane and the three coordinates of such a steady and elementary point were repeatedly registered at 60-Hz frame rates (a standard value for the cameras), for a total of 32,000 repeated measurements of the laser spot. The standard deviations of the registered 3-D coordinates of the measured point were 13.9, 11.5, and 10.6 μm in the x, y, and z directions, respectively, whereas the system's resolution was $\Delta x = \Delta y = \Delta z = 9.33$ μm and the measurement repeatability was ~ 50 μm. This repeatability level was estimated by considering that the system noise is observed in a band of ± 4 levels (9.33 μm each) with an approximately triangular sta-

tistical distribution. The root mean square (rms) noise and the system resolution increase or decrease linearly with the size of the calibration volume; therefore measurement noise is essentially limited by quantization noise.

As a further experiment to determine the performance of the scanning device, two reference solid spheres of different diameters were used. In this case a portion of the solid surface was scanned and acquired. From the registered 3-D range data, the best-fit theoretical sphere was calculated with a least-squares procedure minimizing the average distance between the fitting sphere and the experimental points. First a solid sphere of radius 29.494 ± 0.018 mm, as measured from 20 repeated measurements by a 50-μm resolution caliper, was scanned and acquired. Ten repeated acquisitions of the object were performed (each acquisition consisted of about 3500 points obtained from laser scanning the sphere) and the radius of the best-fit sphere was calculated for each acquisition. The average value of the radius was 29.484 mm with 0.009 mm statistical uncertainty, resulting in good compatibility ($k = 1$ coverage factor) with the corresponding mechanical measurement. The acquisition noise for this 30-mm-radius sphere was almost identical in all the 10 repeated measurements and equal to ~ 170 μm (169 μm as calculated).

The second solid sphere had a radius of 11.133 ± 0.016 mm, again measured from 20 repeated measurements by the same 50-μm resolution caliper. The dimension of this solid sphere was similar to the typical dimension of an ear canal. The radius of the best-fit sphere on the scanned and acquired points was calculated from 10 repeated acquisitions of the object. An average value of 11.147 mm with 0.016-mm statistical uncertainty was obtained, resulting again in good compatibility ($k = 1$ coverage factor) with the corresponding mechanical measurement. Also in this case, the acquisition noise for this 11-mm-radius sphere was almost identical in all 10 repeated measurements and equal to ~ 170 μm (171 μm as calculated).

In all the experiments, the acquisition noise was found to be normally distributed at the significance level $\alpha = 0.01$ (Lilliefors test, $p = 0.1078$).

4.2 Acquisition and Reconstruction of Real Ear Canal Impressions

The proposed reconstruction algorithm was tested on a variety of surfaces scanned and acquired by the system described in Sec. 2 (for examples, see Refs. 1 and 10–12). Here, results obtained from the acquisition and reconstruction of 4 of the 10 real ear canal impressions used as test material are presented.

In particular, Fig. 3(b) shows the set of unorganized range data obtained by 3-D scanning of an ear canal impression with our laser scanning system, whereas Fig. 3(c) shows the mesh obtained after the expansion and uniform resampling of the icosahedron of Fig. 3(a). This mesh is an initial, gross approximation of the original surface S_o. The reconstruction of spatial details of S_o is achieved at the end of the second phase. The triangular mesh of the final reconstructed surface of Fig. 3(d) was obtained after local resampling (second phase) and smoothing (third phase) of the previous mesh. As a result of the local refinement procedure, the mesh in Fig. 3(d) has a greater density of triangles in those regions with
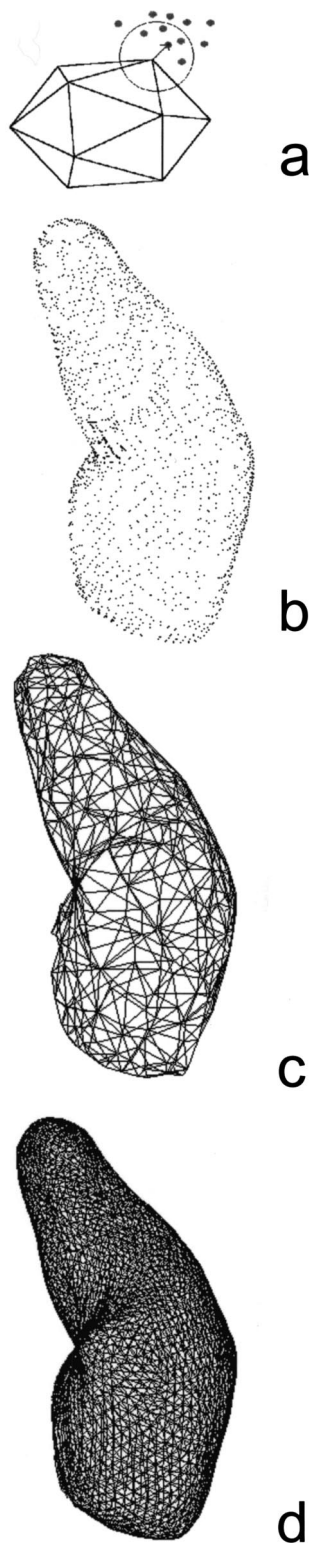
Fig. 3 Pictorial representation of the main phases of the reconstruction algorithm. (a) Each vertex of the geometric model—an icosahedron—is moved toward those points of the range data that fall inside its sphere of neighborhood S_d. (b) The range data used in this example, as obtained by laser scanning the surface of an ear canal impression. (c) The geometric model at its maximal expansion and after three global resamplings (first phase). (d) The final reconstructed model after local resampling (second phase) and smoothing (third phase). For details on the reconstruction algorithm, see Sec. 3.

richer spatial details. The acquisition of the range data of Fig. 3(b), consisting of about 5700 points, took about 2 min for the manual scanning and comparatively negligible time (less than 45 s) for surface reconstruction.

Figure 4 and Fig. 5 show three other examples of the acquisition and reconstruction of real ear impressions.

4.3 *Quantitative Estimation of Reconstruction Accuracy*

To give a quantitative measure of the accuracy of the proposed reconstruction algorithm, a test surface resembling the shape and the dimensions of a typical ear canal impression was artificially generated at the computer. This artificial surface was sampled at a density similar to that achieved during a real acquisition. A Gaussian white noise of rms amplitude ranging from 0.170 mm (i.e., equal to the noise level obtained during a typical acquisition session with the proposed equipment) up to 1 mm was added to the x, y, z coordinates of the vertices of the original test surface. These noisy range data were fed to the reconstruction algorithm and the surface thus reconstructed was compared with the original test surface. As an example, Fig. 6(a) shows the original synthetic test surface, Fig. 6(b) the noisy range data that correspond to an added rms noise of 170 μm, Fig. 6(c) the 3-D solid representation of the noisy version of the test surface, and Fig. 6(d) the reconstructed surface obtained by processing the noisy range data with the proposed algorithm.

To quantitatively estimate the accuracy of the reconstruction, the point-to-point reconstruction error E between the original test surface and the reconstructed surface was computed using Eqs. (1) and (2). Because the original test surface is orientable, we were able to compute a signed reconstruction error E, where E is positive if the reconstructed surface locally falls outside the original test surface and negative otherwise.

Figure 7 shows the distribution of the reconstruction error E between the original test surface (i.e., the noiseless surface) and the reconstructed surface at the different levels of the added noise. In all four tested conditions, the error E had a zero-mean distribution, thus indicating that no bias was introduced by the reconstruction algorithm. Also, the higher the level of the added noise, the wider the distribution of E (i.e., the greater the standard deviation of the distribution).

The results illustrated in Fig. 8 indicate that the rms value of the error E was obviously increasing for increasing values of the added noise, but that it remained significantly lower than the rms value of the noise added to the original test surface. In other words, this means that the reconstruction algorithm was able not only to produce a surface properly fitted to the test surface but also to achieve an improvement in the quality of the reconstructed surface. In particular, at the noise level equal to that obtained during a typical acquisition session (see the results of test 1 in Fig. 8), the error between the reconstructed and the original surface was equal to 0.079 mm, whereas the added rms noise was 0.170 mm. In this case, a >50% noise reduction was thus obtained.

5 Conclusions

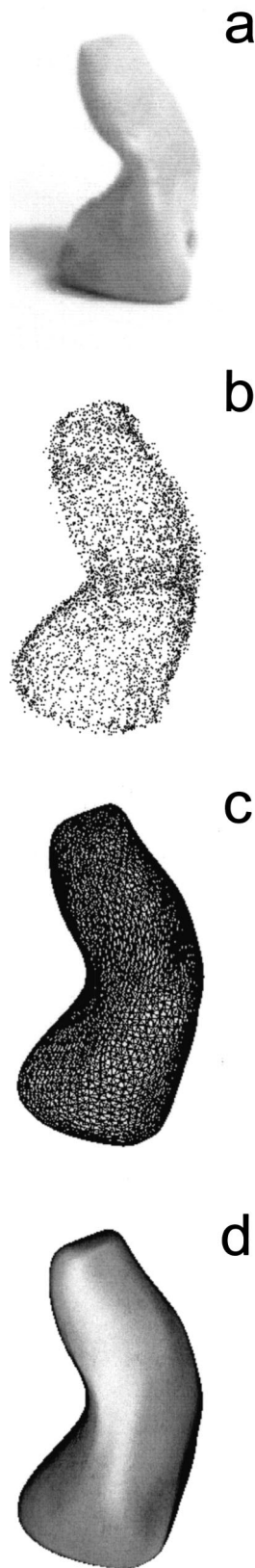We have proposed a new approach for the design of custom-made hearing aid shells. The approach is based on the acqui-

a

b

c

d

Fig. 4 (a) The original ear canal impression ($18\times14\times22$ mm^3). (b) Cloud of acquired points (unorganized range data) obtained by laser scanning the surface of the impression. (c) The final reconstructed surface (wireframe representation). (d) Solid representation of the reconstructed surface shown in (c).
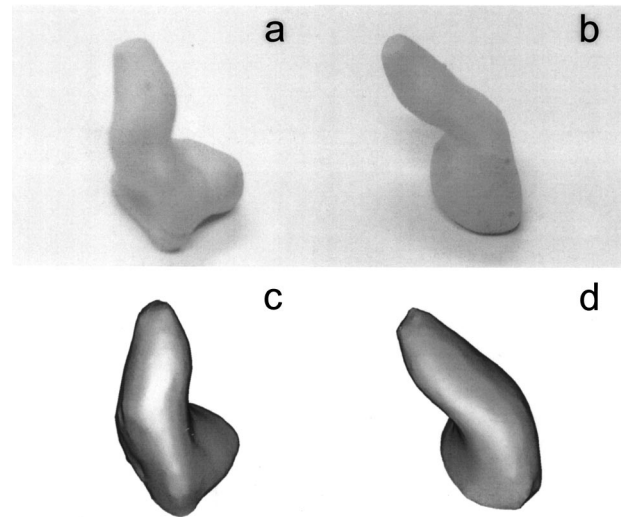

Fig. 5 (a)–(b) Original ear canal impressions; (c)–(d) the final reconstructed surfaces of the impressions shown in (a) and (b).

sition and reconstruction of the surface of ear canal impressions. The whole system is based on direct acquisition of data by laser spot scanning and effective image processing, by expanding and adaptively fitting a regular geometric model, for reconstructing a surface. Different acquisition experiments showed that the scanning equipment has an estimated resolution <10 μm, a repeatability <50 μm, and an acquisition noise of ~170 μm (rms value).

The proposed reconstruction algorithm is adaptive in the sense that the resulting triangular mesh locally minimizes an approximation error function, giving a quantitative estimate of the accuracy of the reconstruction. In this way, it is possible to obtain a nonuniform triangular mesh with a greater density of triangles only in those regions richer in spatial details. As such, the proposed approach overcomes all the problems related to the manipulation and storage of redundant and very dense triangular meshes. Typically, huge triangular meshes need to be simplified to achieve a reduction of points, memory saving, and computational time, while maintaining a given accuracy in the reconstruction (for a survey of mesh simplification methods, see Ref. 13).

When considering real ear canal impressions, the proposed algorithm was able to reconstruct very accurate surfaces showing all the typical anatomical dips and ridges of the real scanned surface. Also, simulations with a synthetic test surface with a shape and dimension similar to a real ear canal impression provided good evidence of the robustness to noise of the proposed reconstruction algorithm, achieving a significant improvement ($>50\%$) between the noisy and the reconstructed surfaces. In particular, the reconstruction error obtained during simulations with levels of noise equal to those achieved during a typical acquisition session (~170 μm) was only ~80 μm.

The proposed system exhibits several advantages with respect to the current manufacturing procedure for the fabrication of hearing aid shells: It is no longer necessary to use postimpression processes because the digitally reconstructed impression can be fed directly to ad hoc CAD/CAM 3-D printing machines, thus achieving a better and quantifiable

Fig. 7 Estimation of reconstruction accuracy. Histogram distribution of the point-to-point reconstruction error *E* between the original surface and the reconstructed surface at the four tested noise levels of (a) 0.177 mm, (b) 0.250 mm, (c) 0.500 mm, and (d) 1 mm.

accuracy in obtaining an exact replica of the ear canal. Also, the entire shell fabrication process would become extremely repeatable and less time-consuming.

In addition, this kind of digital storage of the ear canal impression allows simple and reliable copying or transmission of the model; quality control of the 3-D printing machine (by comparing the 3-D model of the shell with a 3-D scan of the

Fig. 6 Simulations with the test surface. (a) The original test surface (synthesized surface) with a shape and dimensions similar to these of a real ear canal impression. (b) The noisy range data obtained by adding a Gaussian noise of 0.177 mm (rms value) to the coordinates of the vertices of the original test surface in (a). (c) A solid representation of the noisy surface. (d) The reconstructed surface obtained with the proposed algorithm by processing the noisy range data in (b).
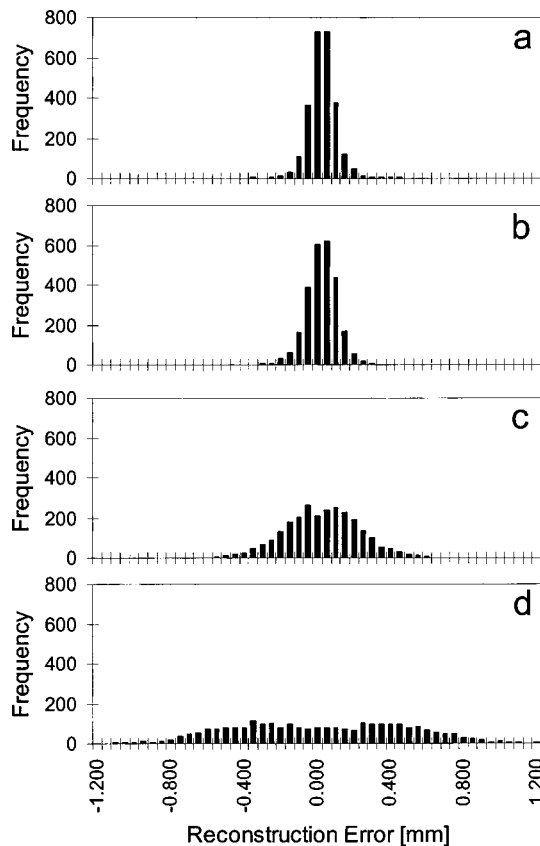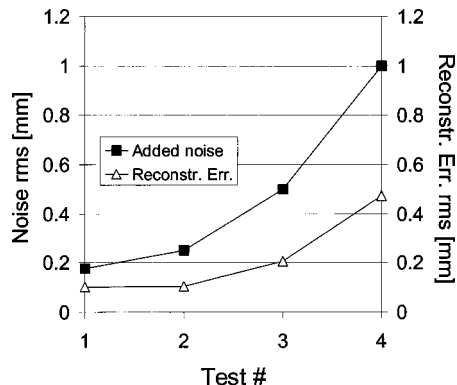
Fig. 8 Estimation of reconstruction accuracy. The two curves show the rms amplitude of the noise added to the original test surface (squares) and the rms reconstruction error (triangles) in the four tested conditions. In particular, the rms reconstruction error was measured from the distributions shown in Fig. 7.

printed shell); quantitative analysis of the fitting of the shell (by comparing the digitized version of the ear canal with a 3-D scanned version of the printed shell); and optimal placement of the electronic module into the 3-D model of the shell to optimize the acoustical features of the hearing aid.

Acknowledgments

References

1. G. Tognola, M. Parazzini, C. Svelto, P. Ravazzani, and F. Grandori, "A fast and reliable system for 3D surface acquisition and reconstruction," *Image Vis. Comput.* **21**, 295–305 (2003).
2. T. Josefsson, E. Nordh, and P.-O. Eriksson, "A flexible high-precision video system for digital recording of motor acts through lightweight reflex markers," *Comput. Methods Programs Biomed.* **49**, 119–129 (1996).
3. J. Montagnat, H. Delingette, and N. Ayache, "A review of deformable surfaces: topology, geometry and deformation," *Image Vis. Comput.* **19**, 1023–1040 (2001).
4. J. V. Miller, D. E. Breen, W. E. Lorensen, R. M. O'Bara, and M. J. Wozny, "Geometrically deformed models," in *Proc. ACM SIGGRAPH Comput. Graph.* **25**, 217–226 (1991).
5. D. J. Williams and M. Shah, "A fast algorithm for active contours and curvature estimation," *Comp. Vis. Graphics, Image Proc.: Image Understanding* **55**, 14–26 (1992).
6. A. J. Bulpitt and N. D. Efford, "An efficient deformable model with a self-optimising mesh," *Image Vis. Comput.* **14**, 573–580 (1996).
7. P. Cignoni, C. Rocchini, and R. Scopigno, "Metro: measuring error on simplified surfaces," *Comp. Graph. Forum* **17**, 167–174 (1998).
8. G. Taubin, "A signal processing approach to fair surface design," in *Proc. ACM SIGGRAPH Comput. Graph.*, 351–358 (1995).
9. G. Taubin, T. Zhang, and G. Golub, "Optimal surface smoothing as filter design," in *Proc. 4th Europ. Conf. Comput. Vis. ECCV'96*, 283–292 (1996).
10. G. Tognola, M. Parazzini, C. Svelto, P. Ravazzani, and F. Grandori, "Three-dimensional laser scanning and reconstruction of ear canal impressions for optimal design of hearing aid shells," in *Proc. IS&T/ SPIE Electronic Imaging 2003* **5009**, 123–130 (2003).
11. G. Tognola, M. Parazzini, P. Ravazzani, F. Grandori, and C. Svelto, "Simple 3D laser scanner for anatomical parts and image reconstruction from unorganized range data," in *Proc. IEEE Instr. Meas. Tech. Conf.* **1**, 171–174 (2002).
12. G. Tognola, M. Parazzini, P. Ravazzani, C. Svelto, and F. Grandori, "3D reconstruction of anatomical surfaces from unorganized range data," in *Proc. IEEE Eng. Med. Biol. Soc. Conf.* **3**, 2534–2536 (2001).
13. P. Cignoni, C. Montani, and R. Scopigno, "Comparison of mesh simplification algorithms," *Comput. Graph.* **22**, 37–54 (1998).